

# Fast and slow dynamics in a nonlinear elastic bar excited by longitudinal vibrations

Nicolas Favrie<sup>a</sup>, Bruno Lombard<sup>b</sup>, Cédric Payan<sup>b</sup>

<sup>a</sup>IUSTI, Aix-Marseille Université, UMR CNRS 7343, 5 rue E. Fermi, 13453 Marseille Cedex 13, France

<sup>b</sup>Laboratoire de Mécanique et d'Acoustique, UPR 7051 CNRS, 31 chemin Joseph Aiguier, 13402 Marseille, France

---

## Abstract

The dynamics of heterogeneous materials, like rocks and concrete, is complex. It includes such features as nonlinear elasticity, hysteresis, and long-time relaxation. This dynamics is very sensitive to microstructural changes and damage. The goal of this paper is to propose a physical model describing the longitudinal vibrations in heterogeneous material, and to develop a numerical strategy to solve the evolution equations. The theory relies on the coupling of two processes with radically different time scales: a fast process at the frequency of the excitation, governed by nonlinear elasticity and viscoelasticity, and a slow process, governed by the evolution of defects. The evolution equations are written as a nonlinear hyperbolic system with relaxation. A time-domain numerical scheme is developed, based on a splitting strategy. The features observed by numerical simulations show qualitative agreement with the features observed experimentally by Dynamic Acousto-Elastic Testing.

**Keywords:** Nonlinear acoustics; time-dependent materials; viscoelasticity; acoustic conditioning; numerical methods; hyperbolic system.

---

## 1. Introduction

Understanding the mechanisms of acoustic nonlinearity in heterogeneous materials is an object of intensive studies [11, 22, 12, 16]. Experimental evidence has shown that media such as rocks and concrete possess an anomalously strong acoustic nonlinearity, which is of great importance for the description of ultrasonic phenomena including damage diagnostics. Besides the widely-studied nonlinear and hysteretic stress-strain relation [15], a long-time relaxation is also reported by most of the authors [29, 30]. This slow dynamics is typically observed in experiments of softening / hardening [25, 26], where a bar is forced by a monochromatic excitation on a time interval, before the source is switched-off. During the experiment, the elastic modulus is measured by Dynamic Acousto-Elastic Testing methods. It can be observed that the elastic modulus decreases gradually (softening), and then it recovers progressively its initial value after the extinction of the source (hardening). The time scales of each stage is much longer than the time scale of the forcing, which justifies the term "slow dynamics".

---

\*Corresponding author. Tel.: +33 491 16 44 13.

Email addresses: nicolas.favrie@univ-amu.fr (Nicolas Favrie), lombard@lma.cnrs-mrs.fr (Bruno Lombard), cedric.payan@univ-amu.fr (Cédric Payan)

Preprint submitted to Wave Motion

December 8, 2014

The modelling of this slow dynamic effect has been investigated by many authors. An essentially phenomenological model is widely used for this purpose: the Preisach-Mayergoyz model (P-M model) based on the integral action of hysteretic elements connecting stress and strain [27, 28, 16]. This model initially arose from the theory of magnetism, where the "hysteron" has a clear physical significance. In elasticity, such a physical interpretation is not available. To overcome this limitation and to develop a rigorous theory, various authors have proposed alternative models based on clear mechanical concepts. To our knowledge, the first physical model of slow dynamics was described in [30], where the relaxation was related to the recovery of microscopic contact impeded by a smooth spectrum of energy barriers. This theory was extended in [2, 3], and recently improved based on the analysis of inter-grain contacts and the resulting surface force potential with a barrier [16]. Another approach was followed in [23], where the author shows that two rough surfaces interacting via adhesion forces yield dynamics similar to that of the fictitious elements of the Preisach-Mayergoyz space [23].

Here, we present an alternative mechanical description of slow dynamics based on the works of Vakhnenko and coauthors [32, 33], where the following scenario is proposed:

- the Young's modulus  $E$  varies with time. One can write  $E(g)$ , where  $g$  is a time-dependent concentration of defects. It is closely related to the notion of damage in solids mechanics. But contrary to what happens in this irreversible case, where  $g$  strictly increases with time, the evolution of  $g$  is reversible. Waiting a sufficiently long time, the initial material properties are recovered;
- at equilibrium, stress  $\sigma$  yields a concentration of defects  $g_\sigma$ . The dependence of  $g_\sigma$  with respect to  $\sigma$  is monotonic;
- out of equilibrium, relaxation times are required for  $g$  to reach  $g_\sigma$ . Whether  $g < g_\sigma$  (increase in the number of defects) or  $g > g_\sigma$  (decrease in the number of defects), Vakhnenko et al state that the time scales differ. The argument is given in section III of [33]: "there are various ways for an already existing crack in equilibrium to be further expanded when surplus tensile load is applied. However, under compressive load a crack, once formed, has only one spatial way to be annihilated or contracted". In both cases, these relaxation times are much longer than the time scale of the excitation, which explains the slow dynamics.

Comparisons with experimental data are given in section V of [33], where the authors reproduced experiments done on Berea sandstone [29]. One current weakness is that no micro-mechanical description of the involved defects has been proposed so far. A possible analogy may be found with populations of open / closed cracks filled with air, equivalent to a population of bubbles that relax towards an equilibrium state, depending on the applied stress [8, 9]. In counterpart, one attractive feature of Vakhnenko's model is that it combines hyperbolic equations and relaxation terms, which constitutes a sound basis of physical phenomena [10].

The present paper is a contribution to the theoretical analysis of this model and to its practical implementation to describe wave motion in damaged media. First, we point out that no mechanisms prevents the concentration of defects from exceeding 1, which is physically unrealistic. We fix this problem by proposing another expression for the equilibrium concentration. Second, the Stokes model describing viscoelasticity behaviour in [33] poorly describes the attenuation in real media, and it is badly suited to time-domain simulations of wave propagation. Instead, we propose a new nonlinear version of the Zener model. This viscoelastic model degenerates correctly towards a pure nonlinear elasticity model when attenuation effects vanish. Moreover,

the usual Zener model in the linear regime is recovered [5]. In practice, this model only requires one physical parameter under the assumption of constant quality factor. Third, hyperbolicity is analyzed. Depending on the chosen model of nonlinear elasticity, a real sound speed may be obtained only on a finite interval of strains; this is true in particular with the widely-used Landau's model.

The main effort of Vakhnenko et al was devoted to the construction of a model of slow dynamics. The resolution of the involved equations was quite rudimentary and not satisfying. Indeed, the equilibrium concentration of defects  $g_\sigma$  was assumed to be known and was imposed (eq (17) in [33]), while it depends on  $\sigma$ . But treating the full coupled nonlinear equations is out of reach of a semi-analytical approach, which explains the strategy of these authors. On the contrary, we propose here a numerical method to integrate the full system of equations, involving the nonlinear elasticity, the hysteretic terms of viscoelasticity, and the slow dynamics. Due to the existence of different time scales, a splitting strategy is followed, ensuring the optimal time step for integration. The full system is split into a propagative hyperbolic part (resolved by a standard scheme for conservation laws) and into a relaxed part (resolved exactly).

Our numerical model is very modular. The various bricks (nonlinear elasticity, viscoelasticity, slow dynamics) can be incorporated easily. Numerical tests validate each part separately. When all the whole bricks are put together, typical features of wave motion in damaged media are observed. The softening / hardening experiments are qualitatively reproduced.

## 2. Physical modeling

In this section, we write the basic components describing the wave motion in a 1D material with damage. The foundations rely on linear elastodynamics, whose equations are recalled in section 2.1. Then, the soft-ratchet model of Vakhnenko and coauthors is introduced and enhanced in section 2.2. The fast dynamics is described in section 2.3, where various known models of nonlinear elasticity are presented, and a nonlinear model of viscoelasticity is proposed. This latter degenerates correctly in the limit cases of linear elasticity or null attenuation.

### 2.1. Linear elastodynamics

In the case of small deformations, the propagation of 1D elastic waves can be described by the following system [1]:

$$\left\{ \begin{array}{l} \frac{\partial v}{\partial t} - \frac{1}{\rho} \frac{\partial \sigma}{\partial x} = \gamma, \end{array} \right. \quad (1a)$$

$$\left\{ \begin{array}{l} \frac{\partial \varepsilon}{\partial t} - \frac{\partial v}{\partial x} = 0, \end{array} \right. \quad (1b)$$

where  $t$  is the time,  $x$  is the spatial coordinate,  $\gamma$  is a forcing term,  $u$  is the displacement,  $v = \frac{\partial u}{\partial t}$  is the velocity,  $\varepsilon = \frac{\partial u}{\partial x}$  is the strain, and  $\sigma$  is the stress. The latter is a function of strain:  $\sigma = \sigma(\varepsilon)$ .

In the linear case, Hooke's law writes  $\sigma = E \varepsilon$ , where  $E$  is the Young's modulus, which is assumed to be constant over time. In the particular case where  $\gamma$  is a Dirac source at  $x_s$  with time evolution  $\mathcal{G}(t)$ , then the exact solution of (1) is straightforward

$$\varepsilon = -\frac{\text{sgn}(x - x_s)}{2c^2} \mathcal{G}\left(t - \frac{|x - x_s|}{c}\right), \quad (2)$$

98 where  $\text{sgn}$  is the sign distribution, and  $c = \sqrt{\frac{1}{\rho} \frac{\partial \sigma}{\partial \varepsilon}} \equiv \sqrt{E/\rho}$  is the speed of sound.

99 The goal of the forthcoming sections is to extend the model (1) in three ways:

- 100 • time variations of  $E$  due to the stress;
- 101 • nonlinear Hooke's law;
- 102 • hereditary effects (viscoelasticity).

103 The time scales for the first effect (variation of  $E$ ) are much greater than for the second and third  
104 effect. This is consequently referred to as *slow dynamics*.

## 105 2.2. Slow dynamics: soft-ratchet model

106 Here we follow the approach taken from [32, 33] with some modifications. The slow dynam-  
107 ics of the medium is assumed to rely on the concentration of activated defects  $g$ , which varies  
108 with  $\sigma$ . In the lowest approximation, the Young's modulus is written:

$$E = \left(1 - \frac{g}{g_{cr}}\right) E^+, \quad (3)$$

109 where  $g_{cr}$  and  $E^+$  are the critical concentration of defects and the maximum possible value of  
110 Young's modulus, respectively (figure 1-(a)). The following constraints hold:

$$0 \leq g \leq g_{cr} \leq 1. \quad (4)$$

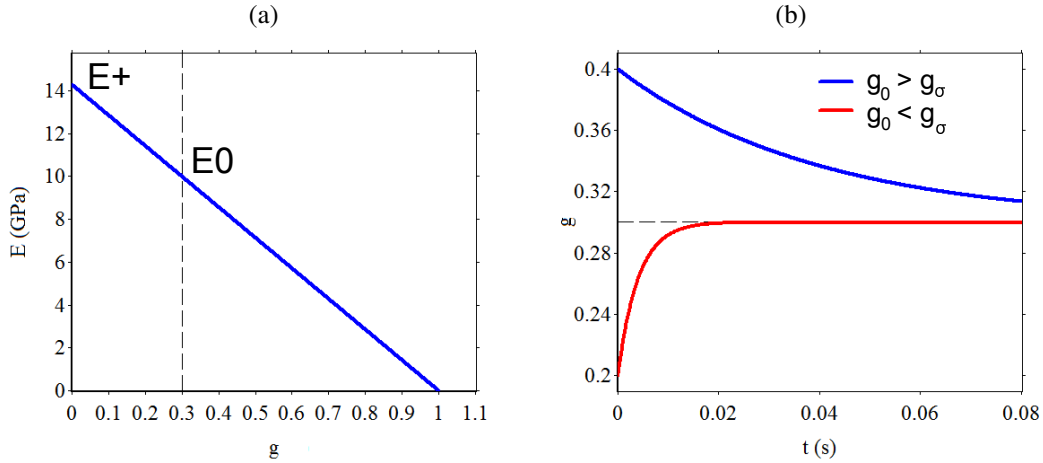


Figure 1: parameters of the slow dynamics. (a): Young's modulus  $E$  in terms of the concentration of defects  $g$  (3), for  $E^+ = 14.28$  GPa; the vertical dotted line denotes the initial concentration of defects  $g_0 = 0.3$  and the corresponding Young's modulus  $E_0 = E(g_0) = 10$  GPa. (b): time evolution of the concentration of defects  $g$  given an equilibrium stress  $\sigma$  and two initial values  $g_0$ ; the horizontal dotted line denotes  $g_\sigma$ .

111 The concentration  $g$  is assumed to evolve to its stress-dependent equilibrium value  $g_\sigma$  at a  
 112 rate  $f_r$  if  $g > g_\sigma$  (restoration), or  $f_d$  if  $g < g_\sigma$  (destruction). This mechanism can be modeled by  
 113 the ordinary differential equation

$$\frac{dg}{dt} = -(f_r H(g - g_\sigma) + f_d H(g_\sigma - g)) (g - g_\sigma), \quad (5)$$

114 where  $H$  is the Heaviside step distribution. The frequencies  $f_r$  and  $f_d$  differ substantially:

$$f_r \ll f_d \ll f_c, \quad (6)$$

115 where  $f_c$  is a typical frequency of the excitation. Figure 1-(b) represents the time evolution of  
 116  $g$ , given a constant equilibrium concentration  $g_\sigma = 0.3$  denoted by a horizontal dotted line. The  
 117 restoration and rupture frequencies are  $f_r = 25$  Hz and  $f_d = 250$  Hz, respectively. Two initial  
 118 value of the concentration of defects are considered:  $g_0 = 0.2$  and  $g_0 = 0.4$ . In both cases,  $g$   
 119 tends towards  $g_\sigma$  with different rates: destruction is much faster than restoration.

120 It remains to define the evolution of  $g_\sigma$  with  $\sigma$ . In [32, 33], the authors propose the expression

$$g_\sigma = g_0 \exp(\sigma/\bar{\sigma}), \quad \bar{\sigma} = \frac{kT}{\nu}, \quad (7)$$

where  $g_0$  is the unstrained equilibrium concentration of defects,  $k$  is the Boltzmann constant,  $T$  is the temperature, and  $\nu$  is a typical volume accounting for a single defect. If  $\sigma > \bar{\sigma} \ln g_{cr}/g_0$ , then  $g_\sigma > g_{cr}$ ; in this case, the concentration may evolve to  $g > g_{cr}$  due to equation (5), which contradicts the second assumption in (4). To remove this drawback and to build a physically realistic expression of  $g_\sigma$ , we enforce (4) together with the following requirements:

$$\left\{ \begin{array}{l} 0 \leq g_\sigma < g_{cr}, \\ g_\sigma(0) = g_0, \\ \lim_{\sigma \rightarrow -\infty} g_\sigma = 0, \\ \lim_{\sigma \rightarrow +\infty} g_\sigma = g_{cr}, \\ \frac{\partial g_\sigma}{\partial \sigma} > 0. \end{array} \right. \quad \begin{array}{l} (8a) \\ (8b) \\ (8c) \\ (8d) \\ (8e) \end{array}$$

121 The simplest smooth function satisfying (8) is

$$g_\sigma = \frac{g_{cr}}{2} \left( 1 + \tanh \left( \frac{\sigma - \sigma_c}{\bar{\sigma}} \right) \right), \quad (9)$$

122 where the central stress is

$$\sigma_c = \bar{\sigma} \tanh^{-1} \left( 1 - 2 \frac{g_0}{g_{cr}} \right). \quad (10)$$

123 Figure 2-(a) illustrates the two expressions of the stress-dependent equilibrium value  $g_\sigma$ : the  
 124 "exponential model" (7), and the "tanh model" (9)-(10). The numerical values are  $g_0 = 0.3$  and  
 125  $\bar{\sigma} = 10^5$  Pa. The two expressions are the same at null stress. But for tractions greater than  
 126 230 kPa, the value of  $g_\sigma$  deduced from (7) exceeds 1, leading to non-physical negative Young's  
 127 modulus. Figure 2-(b) illustrates the influence of  $\bar{\sigma}$  in (9). As  $\bar{\sigma}$  decreases,  $g_\sigma$  may evolve more  
 128 easily towards the extreme values 0 and  $g_{cr}$ , and hence the damage may increase thanks to (5).

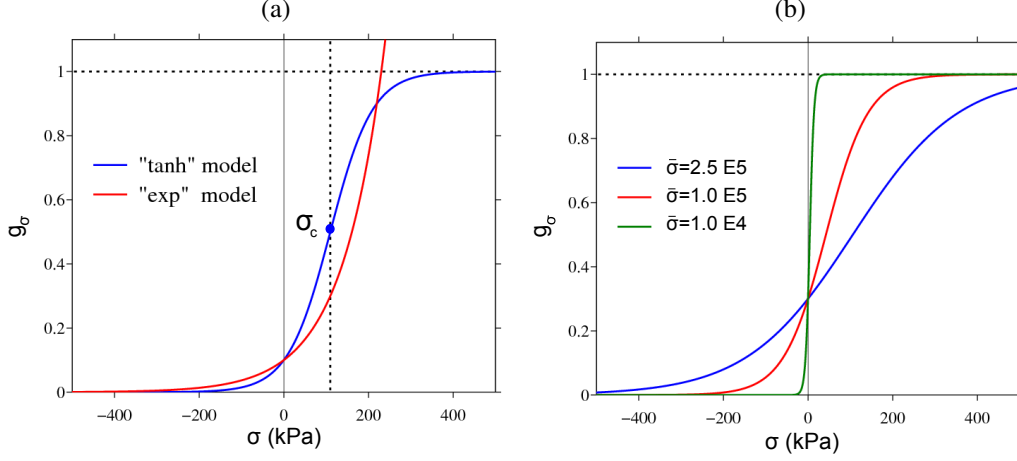


Figure 2: equilibrium concentration of defects  $g_\sigma$  in terms of the applied stress  $\sigma$ . (a): "exponential model" (7) and "tanh model" (9). (b): "tanh model" (9) with various values of  $\bar{\sigma}$ . The horizontal dotted line denotes the critical concentration of defects  $g_{cr}$ ; the vertical dotted line denotes the central stress  $\sigma_c$ .

### 2.3. Fast dynamics: nonlinear viscoelasticity

#### Nonlinear elasticity.

The stress-strain relation is given by a smooth function

$$s \equiv s(\epsilon, K, \mathbf{p}), \quad (11)$$

where  $s$  is the stress,  $\epsilon$  is the strain,  $K$  is a stiffness, and  $\mathbf{p}$  is a set of parameters governing the nonlinearity. No pre-stress is considered;  $K$  is the slope of  $s$  at the origin; lastly,  $s$  is homogeneous of degree 1 in  $K$ . In other words,  $s$  satisfies the following properties:

$$s(0, K, \mathbf{p}) = 0, \quad \frac{\partial s}{\partial \epsilon}(0, K, \mathbf{p}) = K, \quad s(\epsilon, \alpha K, \mathbf{p}) = \alpha s(\epsilon, K, \mathbf{p}). \quad (12)$$

Three models of nonlinear elasticity (11) satisfying (12) are now given and illustrated in figure 3.

**Model 1.** This model is from [33] and mimics the Lennard-Jones potential describing the interaction between a pair of neutral atoms:

$$s(\epsilon, K, \mathbf{p}) = K \frac{d}{r-a} \left( \frac{1}{\left(1 + \frac{\epsilon}{d}\right)^{a+1}} - \frac{1}{\left(1 + \frac{\epsilon}{d}\right)^{r+1}} \right), \quad \mathbf{p} = (r, a, d)^T. \quad (13)$$

The nonlinear parameters are the repulsion and attraction coefficients  $r$  and  $a$  ( $0 < a < r$ ). The strain is bounded below by the maximal allowable closure  $d$ . The function (13) has an extremal point  $\epsilon_c > 0$ , and then it decreases asymptotically towards 0 when  $\epsilon > \epsilon_c$  (figure 3-(a)).

142 Model 2. A third-order Taylor expansion of the model 1 (13) yields

$$s(\epsilon, K, \mathbf{p}) = K \epsilon \left( 1 - \frac{1}{2} (r + a + 3) \frac{\epsilon}{d} + \frac{1}{6} (r^2 + ra + a^2 + 6r + 6a + 11) \left( \frac{\epsilon}{d} \right)^2 \right), \quad \mathbf{p} = (r, a, d)^T. \quad (14)$$

143 The nonlinear parameters are the same than in model 1. But contrary to what happened in model  
144 1, the function (14) is a strictly monotonically increasing function without extremal point (figure  
145 3-(a)). Moreover, the strain is not bounded below.

146 Model 3. The most widely used law in ultrasonic NonDestructive Testing is the so-called Lan-  
147 dau's model [17]

$$s(\epsilon, K, \mathbf{p}) = K \epsilon (1 - \beta \epsilon - \delta \epsilon^2), \quad \mathbf{p} = (\beta, \delta)^T. \quad (15)$$

148 The parameters governing the nonlinear behavior are  $\beta$  and  $\delta$ ; in practice,  $\beta \ll \delta$ . Like what  
149 happens with model 1, the function (15) has extremal points, but it is not bounded below (figure  
150 3-(b)).

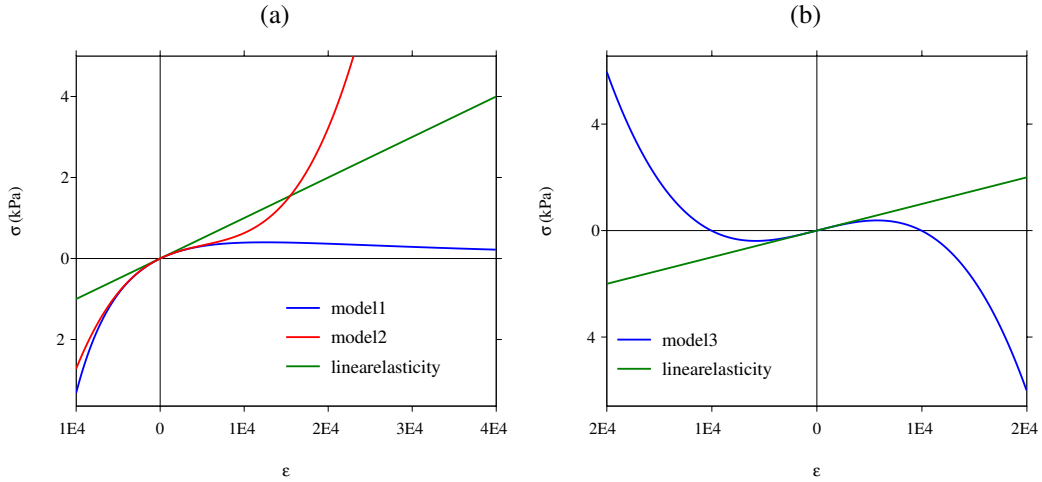


Figure 3: Stress-strain relations for the three models (11). In (a), the dotted lines denote the coordinates of the inflexion point for model 1. The physical parameters are:  $E = 10$  GPa,  $d = 4.3 \cdot 10^{-4}$  m,  $a = 2$ ,  $r = 4$  (models 1 and 2),  $\beta = 100$ ,  $\delta = 10^8$  (model 3).

151 *Viscoelasticity.*

152 To incorporate attenuation, the following criteria are used as a guideline:

153  $C_1$ : when the viscous effects are null, the nonlinear elasticity must be recovered (11);

154  $C_2$ : when a linear stress-strain relation holds, it is necessary to recover the standard linear solid  
155 model (or generalized Zener model), which accurately represents the behavior of usual  
156 solids [5].

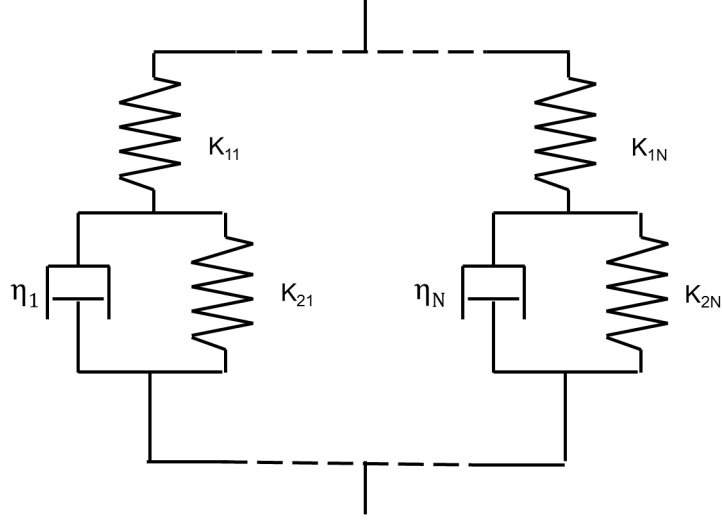


Figure 4: Rheological model of a generalized Zener material.

For this purpose, a system with  $N$  Zener elements connected in parallel is considered (figure 4).  
The total stress acting on the system is

$$\sigma = \sum_{\ell=1}^N \sigma_{1\ell} = \sum_{\ell=1}^N (\sigma_{2\ell} + \sigma_{3\ell}), \quad (16)$$

where the index 1 refers to the springs in series, and indices 2-3 refer to the springs and dashpots in parallel. The strain  $\varepsilon$  is

$$\varepsilon = \varepsilon_{1\ell} + \varepsilon_{2\ell}, \quad \ell = 1, \dots, N. \quad (17)$$

The index 1 springs satisfy nonlinear stress-strain relations (11) with stiffnesses  $K_{1\ell}$ . The parameters  $\mathbf{p}$  governing the nonlinearity (for instance  $\beta$  and  $\delta$  in model 3 (15)) are assumed to be constant and identical for each element. The index 2 springs satisfy linear stress-strain relations with stiffnesses  $K_{2\ell}$ . Lastly, the dashpots satisfy linear Maxwell laws with coefficients of viscosity  $\eta_\ell$ . These laws are summed up as follows:

$$\begin{cases} \sigma_{1\ell}(\varepsilon_{1\ell}) = s(\varepsilon_{1\ell}, K_{1\ell}, \mathbf{p}), & (18a) \end{cases}$$

$$\begin{cases} \sigma_{2\ell}(\varepsilon_{2\ell}) = s(\varepsilon_{2\ell}, K_{2\ell}, \mathbf{0}), & (18b) \end{cases}$$

$$\begin{cases} \sigma_{3\ell}(\varepsilon_{2\ell}) = \eta_\ell \frac{\partial \varepsilon_{2\ell}}{\partial t}. & (18c) \end{cases}$$

To determine the parameters  $K_{1\ell}$ ,  $K_{2\ell}$  and  $\eta_\ell$ , the relaxation times  $\tau_{\sigma\ell}$ ,  $\tau_{\varepsilon\ell}$  and the relaxed modulus  $E_R$  are introduced:

$$\tau_{\sigma\ell} = \frac{\eta_\ell}{K_{1\ell} + K_{2\ell}}, \quad \tau_{\varepsilon\ell} = \frac{\eta_\ell}{K_{2\ell}}, \quad \frac{E_R}{N} = \frac{K_{1\ell} K_{2\ell}}{K_{1\ell} + K_{2\ell}}. \quad (19)$$

On the one hand, a procedure is given in Appendix A to compute the relaxation times in terms of the quality factor  $Q$ . On the other hand,  $E_R$  is related to the unrelaxed Young's modulus  $E$  (3)



165 and to the relaxation times previously determined (see [5]):

$$E_R = \frac{N}{\sum_{\ell=1}^N \frac{\tau_{\varepsilon\ell}}{\tau_{\sigma\ell}}} E. \quad (20)$$

166 Once  $\tau_{\sigma\ell}$ ,  $\tau_{\varepsilon\ell}$  and  $E_R$  are determined, inverting (19) provides the values of the viscoelastic model  
167 in terms of relaxed modulus and relaxation times ( $\ell = 1, \dots, N$ ):

$$K_{1\ell} = \frac{\tau_{\varepsilon\ell}}{\tau_{\sigma\ell}} \frac{E_R}{N}, \quad K_{2\ell} = \frac{\tau_{\varepsilon\ell}}{\tau_{\varepsilon\ell} - \tau_{\sigma\ell}} \frac{E_R}{N}, \quad \eta_\ell = \frac{\tau_{\varepsilon\ell}^2}{\tau_{\varepsilon\ell} - \tau_{\sigma\ell}} \frac{E_R}{N}. \quad (21)$$

168 From (20) and (21), it follows that the viscoelastic parameters depend indirectly on the Young's  
169 modulus  $E$ , and thus depend on  $g$ . In other words, the proposed model of viscoelasticity evolves  
170 with the concentration of defects and thus with the applied stress.

171 In the inviscid case, the stress-strain relation deduced from (16)-(18) makes it possible to  
172 recover the nonlinear elasticity (11), whatever the number  $N$  of relaxation mechanisms:

$$\sigma = s(\varepsilon, E, \mathbf{p}). \quad (22)$$

173 This property is proven in Appendix B.

### 174 3. Mathematical modeling

175 In this section, the basic components describing wave motion in damaged media are put  
176 together and analysed. Section 3.1 collects the various mechanisms (nonlinear elastodynamics,  
177 slow dynamics, hysteresis) into a single system of first-order equations. Two important properties  
178 of this system are addressed in section 3.2: hyperbolicity (finite sound velocity) and decrease in  
179 energy.

#### 180 3.1. First-order system

181 The conservation of momentum (1a) writes

$$\frac{\partial v}{\partial t} = \frac{1}{\rho} \frac{\partial \sigma}{\partial x} + \gamma, \quad (23)$$

182 where  $\gamma$  is a forcing term, and  $\sigma$  is given by (16). The hypothesis of small deformations (1b)  
183 gives

$$\frac{\partial \varepsilon}{\partial t} = \frac{\partial v}{\partial x}. \quad (24)$$

184 Lastly, manipulations on (16), (17) and (18c) yield

$$\frac{\partial \varepsilon_{1\ell}}{\partial t} = \frac{\partial v}{\partial x} + \frac{\sigma_{2\ell}(\varepsilon - \varepsilon_{1\ell}) - \sigma_{1\ell}(\varepsilon_{1\ell})}{\eta_\ell}, \quad \ell = 1, \dots, N. \quad (25)$$

In (25),  $\varepsilon_{1\ell}$  takes the place of the memory variables proposed in [20] and is better suited to nonlinear elasticity. Putting together (23)-(25) and the relaxation equation (5) leads to the first-order system of  $N + 3$  evolution equations

$$\left\{ \begin{array}{l} \frac{\partial v}{\partial t} - \frac{1}{\rho} \frac{\partial \sigma}{\partial x} = \gamma, \end{array} \right. \quad (26a)$$

$$\left\{ \begin{array}{l} \frac{\partial \varepsilon}{\partial t} - \frac{\partial v}{\partial x} = 0, \end{array} \right. \quad (26b)$$

$$\left\{ \begin{array}{l} \frac{\partial \varepsilon_{1\ell}}{\partial t} - \frac{\partial v}{\partial x} = \frac{\sigma_{2\ell}(\varepsilon - \varepsilon_{1\ell}) - \sigma_{1\ell}(\varepsilon_{1\ell})}{\eta_\ell}, \end{array} \right. \quad \ell = 1, \dots, N, \quad (26c)$$

$$\left\{ \begin{array}{l} \frac{dg}{dt} = -(f_r H(g - g_\sigma) + f_d H(g_\sigma - g)) (g - g_\sigma). \end{array} \right. \quad (26d)$$

185 To close the system (26), the following equations are recalled:

- 186 • The total stress  $\sigma$  in (26a) depends on  $\varepsilon_{1\ell}$  via (16), (18a), and a nonlinear law (11):

$$\sigma = \sum_{\ell=1}^N s(\varepsilon_{1\ell}, K_{1\ell}, \mathbf{p}). \quad (27)$$

- 187 • The stress components  $\sigma_{1\ell}$  and  $\sigma_{2\ell}$  in (26c) depend on the stiffnesses  $K_{1\ell}$  and  $K_{2\ell}$  (18a) and  
188 (18b). The latter, as well as the viscosity coefficients  $\eta_\ell$ , depend on the Young modulus  $E$   
189 via (20)-(21), and thus on  $g$ :

$$E = \left(1 - \frac{g}{g_{cr}}\right) E^+. \quad (28)$$

- 190 • The equilibrium value of the defect concentration  $g_\sigma$  in (26d) satisfies (9) and (10):

$$g_\sigma = \frac{g_{cr}}{2} \left(1 + \tanh\left(\frac{\sigma - \sigma_c}{\overline{\sigma}}\right)\right). \quad (29)$$

191 The system (26), together with equations (27)-(29), generalizes the standard equations of linear  
192 elastodynamics (1). It accounts for softening / recovering of Young's modulus, nonlinearity and  
193 viscoelasticity.

194 For the sake of clarity, the vector of  $N + 3$  variables is introduced

$$\mathbf{U} = (v, \varepsilon, \varepsilon_{11}, \dots, \varepsilon_{1N}, g)^T. \quad (30)$$

195 Then the system (26) can be put in the form

$$\frac{\partial}{\partial t} \mathbf{U} + \frac{\partial}{\partial x} \mathbf{F}(\mathbf{U}) = \mathbf{R}(\mathbf{U}) + \mathbf{\Gamma}. \quad (31)$$

196 The flux function  $\mathbf{F}$ , the relaxation term  $\mathbf{R}$ , and the forcing  $\mathbf{\Gamma}$  are

$$\begin{aligned} \mathbf{F}(\mathbf{U}) &= \left(-\frac{\sigma}{\rho}, -v, -v, \dots, -v, 0\right)^T, \\ \mathbf{R}(\mathbf{U}) &= (0, 0, \Delta_1, \dots, \Delta_N, -(f_r H(g - g_\sigma) + f_d H(g_\sigma - g)) (g - g_\sigma))^T, \\ \mathbf{\Gamma} &= (\gamma, 0, \dots, 0, 0)^T, \end{aligned} \quad (32)$$

197 where

$$\Delta_\ell = \frac{\sigma_{2\ell}(\varepsilon - \varepsilon_{1\ell}) - \sigma_{1\ell}(\varepsilon_{1\ell})}{\eta_\ell}. \quad (33)$$

198 To conclude, let us consider the limit-case where the viscoelastic attenuation is neglected. In  
 199 this case, equation (22) states that the stress-strain relations degenerate rigorously towards pure  
 200 nonlinear elasticity, whatever  $N$ .

### 201 3.2. Properties

202 Hyperbolicity is a crucial issue in wave problems - physically, mathematically, and numer-  
 203 ically. It amounts to saying that there exists a real and finite sound velocity  $c$ . This property  
 204 was analysed in [21] for a particular nonlinear stress-strain relation in 3D. In 1D, it reduces to a  
 205 simpler case detailed as follows. Let us define the sound speed  $c$  by

$$c^2 = \sum_{\ell=1}^N c_\ell^2 = \frac{1}{\rho} \sum_{\ell=1}^N \frac{\partial \sigma_{1\ell}}{\partial \varepsilon_{1\ell}}. \quad (34)$$

206 The system (31) is hyperbolic if and only if  $c^2 > 0$  in (34). The proof, as well as sufficient  
 207 conditions on the strain to ensure hyperbolicity, is given in Appendix B. From (34), the local  
 208 elastic modulus  $M$  can be deduced:

$$M = \rho c^2 = \sum_{\ell=1}^N \frac{\partial \sigma_{1\ell}}{\partial \varepsilon_{1\ell}}. \quad (35)$$

209 Note that the Stokes viscoelastic model used in [33] introduces a term  $\frac{\partial^2 v}{\partial x^2}$  in the right-hand side of  
 210 (26c). This Laplacian term destroys the hyperbolic character of the system (31). The viscoelastic  
 211 model used here has therefore better mathematical properties.

212 Now let us examine the spectrum of the relaxation function in (31). Let us consider linear  
 213 stress-strain relations. The parameters  $K_{1\ell}$ ,  $K_{2\ell}$  and  $\eta_\ell$  are "frozen" in (20)-(21), so that they do  
 214 not depend on  $g$  via  $E$  (3). Then, the eigenvalues of the Jacobian matrix  $\mathbf{J} = \frac{\partial \mathbf{R}}{\partial \mathbf{U}}$  are

$$\text{Sp}(\mathbf{J}) = \left\{ 0^2, -f_\xi, -\frac{K_{1\ell} + K_{2\ell}}{\eta_\ell} \right\} = \left\{ 0^2, -f_\xi, -\frac{1}{\tau_{\sigma\ell}} \right\}, \quad \ell = 1, \dots, N, \quad (36)$$

215 (see (19)), with  $f_\xi = f_r$  if  $g > g_\sigma$ ,  $f_\xi = f_d$  if  $g < g_\sigma$ ,  $f_\xi = 0$  else. The proof is detailed in  
 216 Appendix C. Two observations can be made:

- 217 •  $\mathbf{J}$  is definite-negative if the relaxation frequencies  $\tau_{\sigma\ell}$  are positive. The latter parameters  
 218 are deduced from an optimization process based on the quality factor (Appendix A). To  
 219 ensure the energy decrease, it is therefore crucial to perform nonlinear optimization with  
 220 constraint of positivity.
- 221 • The optimization procedure detailed in Appendix A is performed on the frequency range  
 222  $[f_{\min}, f_{\max}]$  surrounding the excitation frequency  $f_c$ . These frequencies satisfy

$$f_{\min} \approx \frac{1}{\max \tau_{\sigma\ell}} < f_c < f_{\max} \approx \frac{1}{\min \tau_{\sigma\ell}}. \quad (37)$$

223 In (37),  $\approx$  are replaced by equalities if a linear optimisation is used [20]. From (6), it  
 224 follows the spectral radius of  $\mathbf{J}$

$$\varrho(\mathbf{J}) = \frac{1}{\min \tau_{\sigma\ell}} \gg f_{\xi}, \quad (38)$$

225 so that the system (31) is stiff.

## 226 4. Numerical modeling

227 In this section, a numerical strategy is proposed to integrate the first-order equations (31).  
 228 For the sake of efficiency, a splitting approach is followed in section 4.1. The original equations  
 229 are splitted into two parts, solved successively: a propagative part (section 4.2) and a relaxation  
 230 part (section 4.3).

### 231 4.1. Splitting

232 To integrate (31), a uniform spatial mesh  $\Delta x$  and a variable time step  $\Delta t^{(n)} \equiv \Delta t$  are intro-  
 233 duced. An approximation  $\mathbf{U}_i^n$  of the exact solution  $\mathbf{U}(x_i = i \Delta x, t_n = t_{n-1} + \Delta t)$  is sought. A first  
 234 strategy is to discretize explicitly the non-homogeneous system (31). But numerical stability  
 235 implies a bound of the form

$$\Delta t \leq \min \left( \frac{\Delta x}{c_{\max}}, \frac{2}{\varrho(\mathbf{J})} \right), \quad (39)$$

236 where  $c_{\max} = \max c_i^n$  is the maximal sound velocity at time  $t_n$ , and  $\varrho(\mathbf{J})$  is the spectral radius of  
 237 the Jacobian of the relaxation term. As deduced from (38), the second bound in (39) is penalizing  
 238 compared with the standard CFL condition  $\Delta t \leq \Delta x / c_{\max}$ .

239 Here we follow another strategy: equation (31) is split into a hyperbolic step

$$\frac{\partial}{\partial t} \mathbf{U} + \frac{\partial}{\partial x} \mathbf{F}(\mathbf{U}) = \mathbf{0} \quad (40)$$

240 and a relaxation step

$$\frac{\partial}{\partial t} \mathbf{U} = \mathbf{R}(\mathbf{U}) + \mathbf{\Gamma}. \quad (41)$$

The discrete operators associated with the discretization of (40) and (41) are denoted  $\mathbf{H}_h$  and  $\mathbf{H}_r$ , respectively. The second-order Strang splitting is used, solving successively (40) and (41) with adequate time increments:

$$\left\{ \begin{array}{l} \mathbf{U}_i^{(1)} = \mathbf{H}_r \left( \frac{\Delta t}{2} \right) \mathbf{U}_i^n, \\ \mathbf{U}_i^{(2)} = \mathbf{H}_h (\Delta t) \mathbf{U}_i^{(1)}, \\ \mathbf{U}_i^{n+1} = \mathbf{H}_r \left( \frac{\Delta t}{2} \right) \mathbf{U}_i^{(2)}. \end{array} \right. \quad (42a)$$

$$\mathbf{U}_i^{(2)} = \mathbf{H}_h (\Delta t) \mathbf{U}_i^{(1)}, \quad (42b)$$

$$\mathbf{U}_i^{n+1} = \mathbf{H}_r \left( \frac{\Delta t}{2} \right) \mathbf{U}_i^{(2)}. \quad (42c)$$

241 Provided that  $\mathbf{H}_h$  and  $\mathbf{H}_r$  are second-order accurate and stable operators, the time-marching (42)  
 242 gives a second-order accurate approximation of the original equation (31) [18].

#### 243 4.2. Hyperbolic step

244 The homogeneous equation (40) is solved by a conservative scheme for hyperbolic systems  
245 [18]

$$\mathbf{U}_i^{n+1} = \mathbf{U}_i^n - \frac{\Delta t}{\Delta x} (\mathbf{F}_{i+1/2} - \mathbf{F}_{i-1/2}). \quad (43)$$

246 Many sophisticated schemes can be used for this purpose [19]. For the sake of simplicity and  
247 robustness, the Godunov scheme is used here. The numerical flux function  $\mathbf{F}_{i+1/2}$  is computed  
248 using the Rusanov method [31]

$$\mathbf{F}_{i+1/2} = \frac{1}{2} \left( \mathbf{F}(\mathbf{U}_{i+1}^n) + \mathbf{F}(\mathbf{U}_i^n) - \lambda_{i+1/2}^n (\mathbf{U}_{i+1}^n - \mathbf{U}_i^n) \right), \quad (44)$$

249 where  $\mathbf{F}$  is the flux function (32), and the diffusion parameter  $\lambda_{i+1/2}^n$  is given by the Davis ap-  
250 proximation [7]

$$\lambda_{i+1/2}^n = \max(c_i^n, c_{i+1}^n). \quad (45)$$

251 The Godunov scheme is first-order accurate and stable under the usual Courant-Friedrichs-Lewy  
252 (CFL) condition

$$\Delta t = \frac{\alpha \Delta x}{c_{\max}}, \text{ with } \alpha \leq 1. \quad (46)$$

#### 253 4.3. Relaxation step

Let us denote  $\bar{\mathbf{U}} = (\varepsilon, \varepsilon_{11}, \dots, \varepsilon_{1N})$  and  $\bar{\mathbf{R}}$  the restriction of  $\mathbf{R}(\mathbf{U})$  to the strain components  
(32)-(33). The ordinary differential equation (41) can then be written

$$\begin{cases} \frac{\partial v}{\partial t} = \gamma, & (47a) \end{cases}$$

$$\begin{cases} \frac{\partial \bar{\mathbf{U}}}{\partial t} = \bar{\mathbf{R}}(\bar{\mathbf{U}}), & (47b) \end{cases}$$

$$\begin{cases} \frac{dg}{dt} = -(f_r H(g - g_\sigma) + f_d H(g_\sigma - g)) (g - g_\sigma), & (47c) \end{cases}$$

254 The viscoelastic parameters in the relaxation function  $\bar{\mathbf{R}}$  depend implicitly on  $g$  (see section 2.3),  
255 which complicates the resolution of (47a). However, one can take advantage of the scaling (6).  
256 Indeed,  $\varepsilon$  and  $\varepsilon_{1\ell}$  evolve much faster than  $g$ , so that the viscoelastic parameters  $K_{1\ell}$ ,  $K_{2\ell}$ ,  $\eta_\ell$  are  
257 almost constant on a time step. Consequently, they are "freezed" and the three equations in (47)  
258 can be solved separately.

259 The half-time step in the relaxation steps (42a)-(42c) is denoted by  $\tau = \frac{\Delta t}{2}$ . One details the  
260 time-stepping from  $t_n$  to the first intermediate step (42a); adaptation to the third intermediate step  
261 (42c) is straightforward.

262 The first equation (47a) is integrated using the Euler method:

$$v_i^{n+1} = v_i^{(1)} + \Delta t \gamma(i, t_n). \quad (48)$$

263 To integrate the second equation (47b), a first-order Taylor expansion of  $\bar{\mathbf{R}}(\bar{\mathbf{U}})$  is performed

$$\frac{\partial}{\partial t} \bar{\mathbf{U}} \approx \bar{\mathbf{R}}(\bar{\mathbf{0}}) + \frac{\partial \bar{\mathbf{R}}}{\partial \bar{\mathbf{U}}}(\bar{\mathbf{0}}) \bar{\mathbf{U}} = \bar{\mathbf{J}} \bar{\mathbf{U}}, \quad (49)$$

where  $\bar{\mathbf{J}}$  is the Jacobian matrix (C.2); the nullity of stress at zero strain has been used (18a). Then (49) is solved exactly, leading to the relaxation operator

$$\bar{\mathbf{U}}_i^{(1)} = e^{\bar{\mathbf{J}}\tau} \bar{\mathbf{U}}_i^n \quad (50)$$

with the matrix exponential

$$e^{\bar{\mathbf{J}}\tau} = \begin{pmatrix} 1 & 0 & \cdots & 0 \\ \frac{E_{21}}{E_{11} + E_{21}} \left(1 - e^{-\frac{E_{11}+E_{21}}{\eta_1}\tau}\right) & e^{-\frac{E_{11}+E_{21}}{\eta_1}\tau} & & \\ \vdots & & \ddots & \\ \frac{E_{2N}}{E_{1N} + E_{2N}} \left(1 - e^{-\frac{E_{1N}+E_{2N}}{\eta_N}\tau}\right) & & & e^{-\frac{E_{1N}+E_{2N}}{\eta_N}\tau} \end{pmatrix}. \quad (51)$$

Lastly, the third equation (47c) is solved exactly. The grid value  $g_{\sigma i}$  is evaluated thanks to (9). Setting

$$f_\xi = \begin{cases} f_r & \text{if } g_i^n \geq g_{\sigma i}^n, \\ f_d & \text{if } g_i^n < g_{\sigma i}^n, \end{cases} \quad (52)$$

leads to

$$g_i^{(1)} = g_{\sigma i}^n + (g_i^n - g_{\sigma i}^n) e^{-f_\xi \tau}. \quad (53)$$

The integrations (50), (48) and (53) are unconditionally stable. As a consequence, the splitting (42) is stable under the CFL condition (46).

#### 4.4. Summary of the algorithm

The numerical method can be divided in two parts:

##### 1. initialisation

- bulk modulus  $\rho$ , Young's modulus  $E = E_0 = \rho c_\infty^2$ ;
- soft-ratchet coefficients  $g_{cr} = 1$ ,  $g = g_0$ ,  $f_r$ ,  $f_d$ ,  $\bar{\sigma}$ ;
- maximum Young's modulus  $E^+$  (3)
- nonlinear coefficients (e.g.  $\beta$  and  $\delta$  in (15));
- quality factor  $Q$ , frequency range of optimization  $[f_{\min}, f_{\max}]$ , number of relaxation mechanisms  $N$ ;
- optimization of the viscoelastic coefficients (Appendix A);

##### 2. time-marching $t_n \rightarrow t_{n+1}$ , $x_i = i \Delta x$ ( $n = 0, \dots, N_t$ , $i = 1, \dots, N_x$ )

- physical and numerical parameters
  - Young's modulus  $E$  (3), viscoelastic parameters  $E_R$  (20),  $K_{1\ell}$ ,  $K_{2\ell}$  and  $\eta_\ell$  (21);
  - partial stresses  $\sigma_{1\ell}$  (18a) and total stress  $\sigma$  (16);
  - sound velocity  $c$  (34) and (B.6), maximal velocity  $c_{\max}$ ;
  - time step  $\Delta t$  (46);
- relaxation step  $\mathbf{H}_r$  (42a)
  - strains (50) and (51);

- velocity  $v$  (48);
- concentration of defects at equilibrium  $g_\sigma$  (9) and out of equilibrium  $g$  (53);
- hyperbolic step  $\mathbf{H}_h$  (42b)
  - coefficient  $\lambda_{i+1/2}$  of Davis (45);
  - computation of the flux  $\mathbf{F}$  (32), e.g., by the Rusanov flux  $\mathbf{F}_{i+1/2}$  (44);
  - time-marching of the conservative scheme (43);
- relaxation step  $\mathbf{H}_r$  (42c).

## 5. Numerical experiments

### 5.1. Configuration

$\rho$ (kg/m <sup>3</sup> )	$E_0$ (GPa)	$g_0$	$f_r$ (Hz)	$f_d$ (Hz)	$\overline{\sigma}$ (GPa)	$\beta$	$\delta$	$Q$
2054	2.21	0.1	25	250	0.1	40	$3.5 \cdot 10^6$	20

Table 1: Physical parameters.

The physical parameters are detailed in table 1. Depending on the test, some of these parameters are modified. In the limit-case of linear elasticity, the sound velocity is  $c = \sqrt{E/\rho} = 3280$  m/s. The maximal CFL number is  $\alpha = 0.95$  in (46). The mesh size is  $\Delta x = 4 \cdot 10^{-3}$  m. Depending on the test, two lengths of domain are considered. For each test, a receiver put at  $x_r = 0.2$  m stores the numerical solution at each time step.

The wave fields are excited by a punctual source at  $x_s = 10^{-2}$  m, with a central frequency  $f_c = 10$  kHz. Depending on the expression of the forcing  $\gamma$  in (26c), it is possible to deduce the magnitude of the maximal strain  $\varepsilon_{\max}$  emitted by the source in the limit-case of linear elasticity (2):

$$\varepsilon_{\max} = \frac{1}{2c^2} \max \mathcal{G}(t). \quad (54)$$

The Landau model for nonlinear elasticity is used (15). The coefficient  $\beta$  is much smaller than  $\delta$ . The critical value of strain that ensures hyperbolicity (B.5) is  $\varepsilon_c = 3.08 \cdot 10^{-4}$ . The viscoelastic effects are described by  $N = 4$  relaxation mechanisms. The relaxation times  $\tau_{\sigma\ell}$  and  $\tau_{\varepsilon\ell}$  (19) are computed by optimization on the frequency range  $[f_{\min} = f_c/10, f_{\max} = f_c \times 10]$  (see Appendix A); they are given in table 2.

	$\ell = 1$	$\ell = 2$	$\ell = 3$	$\ell = 4$
$\tau_{\sigma\ell}$ (s)	$1.16 \cdot 10^{-3}$	$2.05 \cdot 10^{-4}$	$4.49 \cdot 10^{-5}$	$7.75 \cdot 10^{-6}$
$\tau_{\varepsilon\ell}$ (s)	$1.53 \cdot 10^{-3}$	$2.49 \cdot 10^{-4}$	$5.50 \cdot 10^{-5}$	$1.06 \cdot 10^{-5}$

Table 2: Relaxation times for a quality factor  $Q = 20$ . Optimization with  $N = 4$  relaxation mechanisms on the frequency range [1 kHz, 100 kHz].

### 5.2. Test 1: nonlinear elastodynamics

In the first test, the viscoelasticity is neglected, and the activation / restoration of defects is annihilated:  $f_r = f_d = 0$  Hz. This test corresponds to the example 12 of [34]. Our goal is to

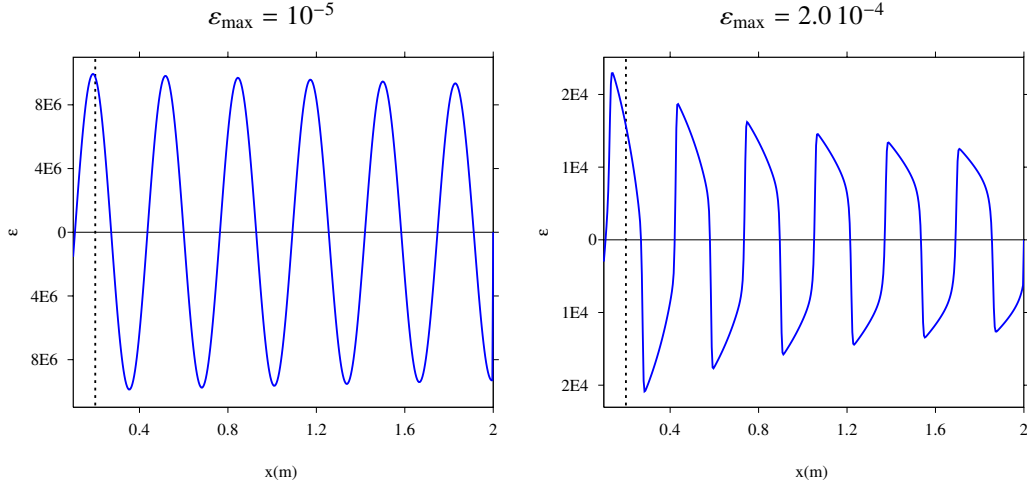


Figure 5: test 1. Snapshot of the strain after 400 time steps, for two amplitudes of the excitation. The vertical dotted line denotes the location  $x_r$  of the receiver.

show typical features of wave propagation in purely nonlinear elastic media. The source is a monochromatic excitation:

$$\mathcal{G}(t) = A \sin(\omega_c t) H(t), \quad (55)$$

where  $A$  is the magnitude of the forcing, and  $\omega_c = 2\pi f_c$ . From (54) and (55), it is possible to estimate the maximal strain  $\varepsilon_{\max}$  emitted by the source in the linear elastic case. The domain of propagation is  $L_x = 2$  m long and is discretized onto 400 grid nodes.

Figure 5 displays the spatial evolution of  $\varepsilon$  after 400 time steps. For  $\varepsilon_{\max} = 10^{-5}$ , almost no distortion of the wave is seen. On the contrary,  $\varepsilon_{\max} = 2.0 \cdot 10^{-4}$  yields a high distortion as the wave propagates. Shocks, as well as the attenuation due to the intersection of characteristic curves [18], are observed.

Figure 6 displays the time evolution of the strain recorded at the receiver (vertical dotted line in Figure 5) for  $\varepsilon_{\max} = 2.0 \cdot 10^{-4}$ . The normalized amplitudes of the Fourier series decomposition show a typical feature of cubic nonlinear elasticity: the spectrum involves mainly odd harmonics [13].

### 5.3. Test 2: linear viscoelasticity

The goal of the second test is to validate the numerical modeling of attenuation. For this purpose, a linear stress-strain relation is chosen ( $\beta = \delta = 0$ ), and the activation / restoration of defects is still annihilated ( $f_r = f_d = 0$  Hz). Consequently, the system (26) simplifies into

$$\begin{cases} \frac{\partial v}{\partial t} - \frac{1}{\rho} \frac{\partial \sigma}{\partial x} = \gamma, & (56a) \end{cases}$$

$$\begin{cases} \frac{\partial \varepsilon}{\partial t} - \frac{\partial v}{\partial x} = 0, & (56b) \end{cases}$$

$$\begin{cases} \frac{\partial \varepsilon_{1\ell}}{\partial t} - \frac{\partial v}{\partial x} = \frac{K_{2\ell}}{\eta_\ell} (\varepsilon - \varepsilon_{1\ell}) - \frac{K_{1\ell}}{\eta_\ell} \varepsilon_{1\ell}. & (56c) \end{cases}$$



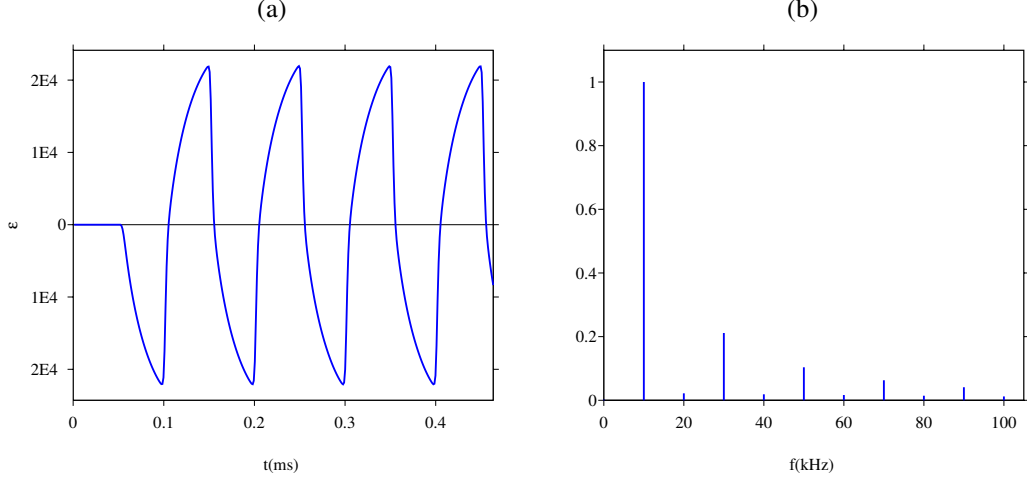


Figure 6: test 1. Time history of the strain at the receiver at  $x_r$  (a), normalized Fourier coefficients (b). The amplitude of the excitation is  $\varepsilon_{\max} = 2.0 \cdot 10^{-4}$ .

The domain of propagation is  $L_x = 2$  m long and is discretized onto 400 grid nodes. The time evolution of the source is a truncated combination of sinusoids with  $C^6$  smoothness:

$$\mathcal{G}(t) = \begin{cases} \sum_{m=1}^4 a_m \sin(b_m \omega_c t) & \text{if } 0 \leq t \leq \frac{1}{f_c}, \\ 0 & \text{otherwise,} \end{cases} \quad (57)$$

with parameters  $b_m = 2^{m-1}$ ,  $a_1 = 1$ ,  $a_2 = -21/32$ ,  $a_3 = 63/768$  and  $a_4 = -1/512$ . Five receivers are put at abscissae  $x_r = 0.5 + 0.3(j-1)$ , with  $j = 1, \dots, 5$ .

Figure 7-(a) shows a seismogram of the velocity recorded at the receivers. Attenuation and dispersion of the waves is clearly observed. Figure 7-(b) compares the numerical solution with the semi-analytical solution after 400 time steps. The computation of the semi-analytical solution is described in Appendix D; it is numerically evaluated with  $N_f = 512$  Fourier modes, with a frequency step  $\Delta f = 200$  Hz. Good agreement is observed between numerical and exact values. The attenuation is slightly overestimated by the scheme, due to the numerical diffusion of the Godunov scheme. This numerical artifact can be fixed by choosing a higher-order scheme [31].

#### 5.4. Test 3: softening / recovering

The goal of the third test is to illustrate the softening / recovering of the elastic modulus, and to validate the numerical modeling of this phenomenon. For this purpose, linear elasticity is assumed and the viscoelasticity is neglected ( $\beta = \delta = 0$ ,  $Q = +\infty$ ). Even if a linear stress-strain relation is used, the evolution problem (26) is nonlinear by virtue of (26d), (28) and (29). Like in test 1, the source is monochromatic; but is switched off after a time  $t^*$ :

$$\mathcal{G}(t) = A \sin(\omega_c t) (H(t) - H(t^*)). \quad (58)$$

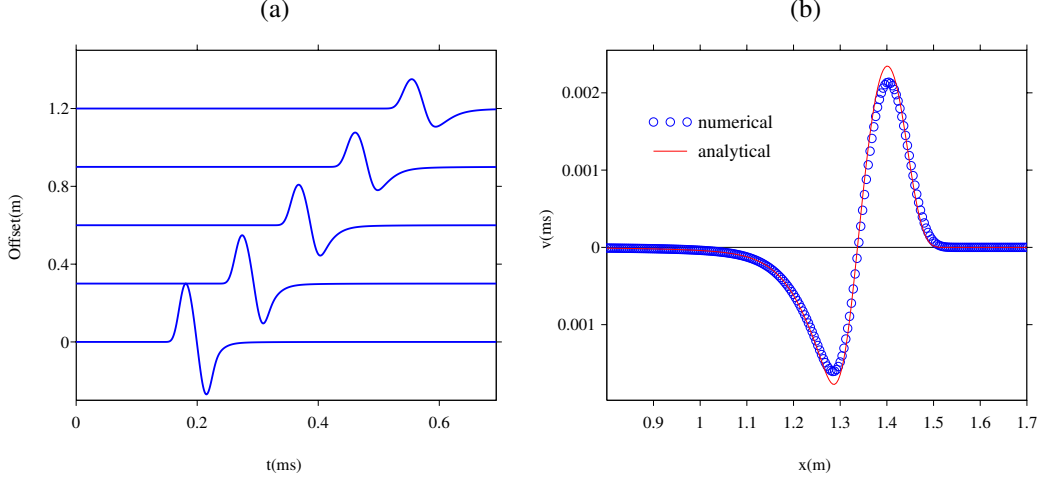


Figure 7: test 2. Wave propagation in a viscoelastic medium. (a): time evolution of  $v$  at a set of receivers; (b): snapshot of  $v$  at  $t = 0.46$  ms, and comparison between the numerical and the semi-analytical solution.

As long as the source is switched on ( $0 < t < t^*$ ), the equilibrium concentration of defects increases from the initial value  $g_0$  up to  $g^* = g(t^*)$ . At the same time, the Young's modulus decreases from  $E_0$  to  $E^*$  via (3).

For  $t > t^*$ , the waves go out of the domain, and the elastodynamic fields vanish. From (29) and (10),  $\sigma = 0$  implies that the equilibrium concentration of defects becomes  $g_\sigma = g_0$ . As a consequence, the ordinary differential equation (ODE) (26d) describing the evolution of defects simplifies into

$$\begin{cases} \frac{dg}{dt} = -f_r(g - g_0), \\ g(t^*) = g^*. \end{cases} \quad (59)$$

The solution of (59) is

$$g(t) = g_0 + (g^* - g_0) e^{-f_r(t-t^*)}. \quad (60)$$

Equation (60) is injected into (3), which gives the time evolution of the Young's modulus during the recovering process ( $t \geq t^*$ ):

$$E(t) = E_0 - \frac{1}{g_{cr}} (g^* - g_0) e^{-f_r(t-t^*)} E^+. \quad (61)$$

The domain of propagation is  $L_x = 0.4$  m long and is discretized onto 100 grid nodes. The maximal strain is  $\varepsilon_{\max} = 10^{-5}$ . Time integration is performed up to  $t = 460$  ms. Figure 8 shows the time evolution of the elastic modulus  $M \equiv E$  (35); this equality occurs only because a linear stress-strain relation is assumed. The numerical values of  $M$  are shown from the beginning of the simulation, whereas the exact values of  $E$  (61) are shown from  $t^*$ . For the sake of clarity, the values are shown only each 5000 time steps. Logically, the elastic modulus decreases as long as the source is switched on (softening), and then increases up to its initial value (recovering).

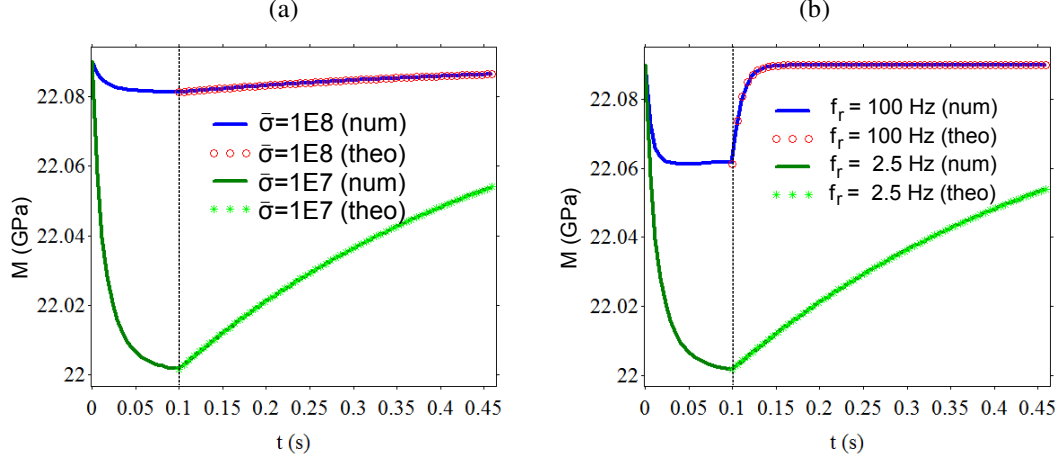


Figure 8: test 3. Time evolution of the elastic modulus  $M$  (35) at  $x_r$ . (a): influence of the central stress  $\bar{\sigma} = 10^8$  Pa and  $10^7$  Pa. (b): influence of the frequency of restoration  $f_r = 2.5$  Hz and 100 Hz. The vertical dotted line denotes the time  $t^*$  where the source is switched off.

Figure 8-(a) illustrates the influence of the central stress on the evolution of  $M$ :  $\bar{\sigma} = 10^8$  Pa or  $10^7$  Pa (the other parameters are those of table 1). According to the Vakhnenko's expression (7), these values correspond to spherical defects of radius  $2.13 \cdot 10^{-10}$  m and  $4.59 \cdot 10^{-10}$  m, respectively. In both cases, equilibrium has been reached at  $t^*$ . The lower value of  $\bar{\sigma}$  yields a greater variation of the elastic modulus. This property follows from (9): as  $\bar{\sigma}$  decreases, the curve  $g \rightarrow g_\sigma$  stiffens and tend towards a Heaviside step function. Consequently, greater values of  $g_\sigma$  are obtained when  $\bar{\sigma}$  is smaller. This implies a greater evolution of  $g$  (5), and hence of  $E$  (3).

Figure 8-(b) illustrates the influence of the frequency of restoration on the evolution of  $M$ :  $f_r = 2.5$  Hz or 100 Hz (the other parameters are those of table 1). The lowest value of  $f_r$  yields a greater variation of the elastic modulus. This is a consequence of the competition between restoration (with frequency  $f_r$ ) and destruction (with frequency  $f_d$ ). When  $f_r$  is too low compared with  $f_d$ , restoration has almost no time to occur during one period  $T = 1/f_c$ , and destruction plays a preponderant role.

#### 5.5. Test 4: full model

The fourth and last test incorporates all the physical mechanisms of the model: nonlinear stress-strain law, viscoelasticity, activation / restoration of defects. The domain is  $L_x = 0.4$  m long and is discretized onto 100 grid nodes. The source is a monochromatic excitation (55). Time integration is performed during  $5 \cdot 10^4$  time steps. The fields are recorded at  $x_r$ .

Figure 9-(a) illustrates the influence of viscoelasticity on the stress-strain law. When viscous effects are neglected ( $Q = +\infty$ , where  $Q$  is the quality factor), the behavior induced by the Landau law (15) is observed. Moreover, the scaling (6) induces that the evolution of defects on one cycle is insufficient to provide a measurable hysteretic effect. On the contrary, hysteresis is obtained when viscoelasticity is accounted for ( $Q = 20$ ). Figure 9-(b) mimics the simulation of test 3, where the source is switched-on and off. But contrary to test 3, a nonlinear stress-strain

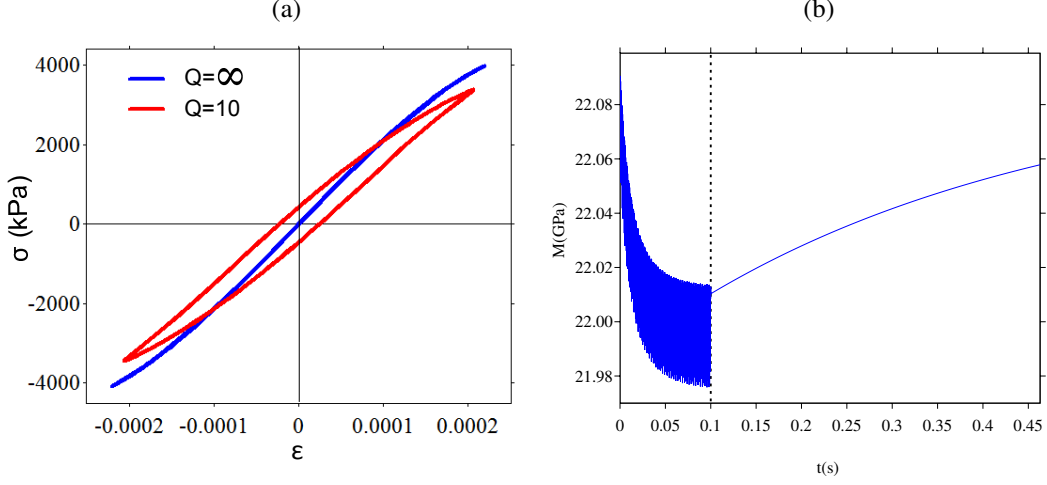


Figure 9: test 4. (a): stress-strain curves at  $x_r$  for different quality factor  $Q$  and a forcing amplitude  $\epsilon_{\max} = 2.0 \cdot 10^{-4}$ . (b): time evolution of the elastic modulus; the vertical dotted line denotes the time  $t^*$  when the source is switched off.

relation is used. Large oscillations up to  $t^*$  can be observed, contrary to what can be seen in figure 8.

Figure 10 displays the relative variation of the elastic modulus  $\Delta M = (M - M_0)/M_0$  in terms of the strain, for various amplitudes of the forcing. Three observations can be made. First, nonlinear curves are obtained, which is a signature of the nonlinear stress-strain relation. Second,  $\Delta M$  increases with  $\epsilon_{\max}$ : softening increases monotonically with the forcing. Third and last, loops are obtained if and only if viscoelasticity is incorporated (c-d). These three features are qualitatively similar to those obtained experimentally [25, 26].

## 5.6. Conclusion

We have proposed a one-dimensional model that captures the behavior of real media under longitudinal bar excitation, including the following features: nonlinear elasticity; softening / recovering of the elastic modulus; hysteretic evolution of the elastic modulus with the strain. The proposed model is very modular. It involves three different bricks which can be used also independently: see for instance the numerical experiments in section 5, in which are considered various combinations of elasticity, attenuation and slow dynamics. Experimentally, the parameters corresponding to each mechanisms can be identified separately:

- the measure of nonlinear elastic parameters is described in many books [11, 13];
- the measure of the quality factor must be performed in the linear regime. See the reference book [4] for a description of an experimental protocol;
- lastly, measuring the parameters of the slow dynamics is detailed in many papers cited in the bibliography. The current challenge is to link the physical observations to the parameters of Vakhnenko's model. Our ambition, with the present paper, is to provide experi-

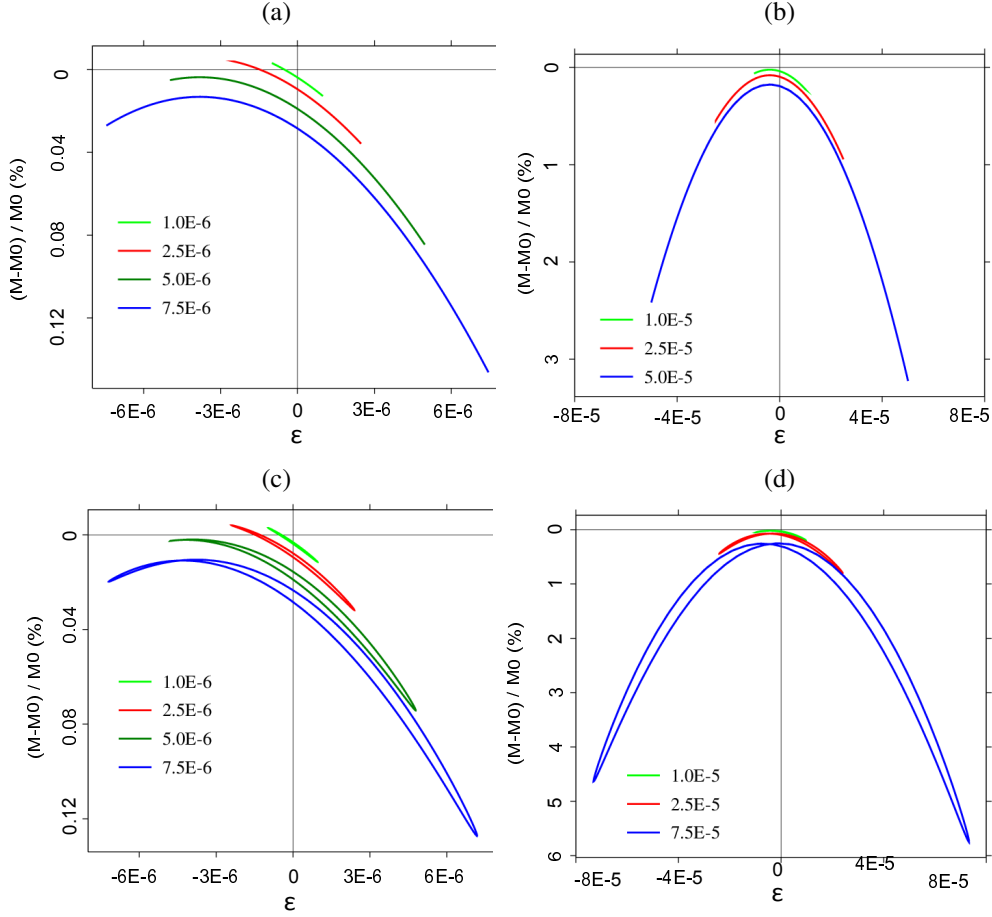


Figure 10: test 4. Relative variations in the elastic modulus  $M$  for various amplitudes of forcing  $\varepsilon_{\max}$ , from  $10^{-6}$  to  $7.5 \cdot 10^{-5}$ . Top (a-b): without viscoelasticity; bottom (c-d): with viscoelasticity.

menters with a tool for testing various sets of parameters, and hence testing the validity of Vakhnenko's model.

A major interest of the numerical approach is the possibility to tackle with variable coefficients in space, which is representative of localized defects [24]. In particular, a random initial distribution of defects  $g_0(x)$  can be considered straightforwardly.

Many improvements can be investigated, to mention but a few. More sophisticated models can be built quite naturally, considering for instance relaxation of the nonlinear coefficients  $\mathbf{p}$  in (18a), or a nonlinear law in (18b). Concerning the numerical simulations, higher-order schemes (such as WENO schemes [18]) can easily be adapted to the proposed formulation. Lastly, theoretical analyses should be done to prove rigorously the well-posedness of the model and its thermodynamic properties.

Work is currently proceeding along two directions. First, numerical simulations are being done to recover quantitatively the experimental results of the literature [25, 26]. Second, the extension of this model to 2D and 3D geometries is under progress.

## Appendix A. Parameters of the viscoelastic model

Standard calculations on (16), (18) and (19) yield the reciprocal of the quality factor  $Q$  [5]

$$Q^{-1}(\omega) = \left( \sum_{\ell=1}^N \frac{\omega(\tau_{\varepsilon\ell} - \tau_{\sigma\ell})}{1 + \omega^2 \tau_{\sigma\ell}^2} \right) / \left( \sum_{\ell=1}^N \frac{1 + \omega^2 \tau_{\varepsilon\ell} \tau_{\sigma\ell}}{1 + \omega^2 \tau_{\sigma\ell}^2} \right). \quad (\text{A.1})$$

Optimizing  $Q^{-1}$  towards a given law (for instance a constant quality factor on a frequency range of interest  $[f_{\min}, f_{\max}]$ ) provides a means to determine  $\tau_{\sigma\ell}$  and  $\tau_{\varepsilon\ell}$  [20]. Here an optimization with constraint is applied to ensure positive values of  $\tau_{\sigma\ell}$  and  $\tau_{\varepsilon\ell}$ , as required by the decrease in energy (see section 3.2). See [6] for details about such an optimization.

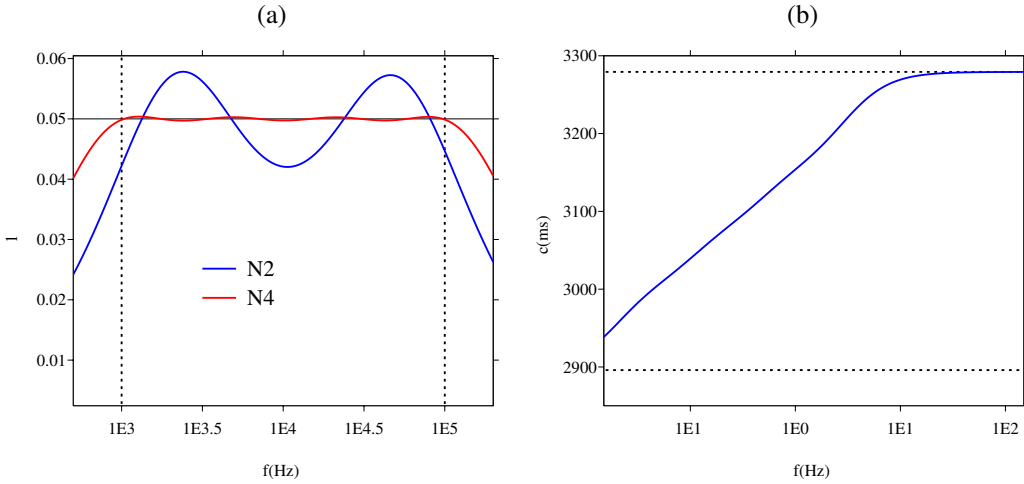


Figure A.11: Properties of the viscoelastic model in the linear regime. (a): reciprocal of the quality factor  $Q = 20$  (A.1). The constant exact value is denoted by a horizontal line; the values obtained after optimization with  $N = 2$  and  $N = 4$  relaxation mechanisms are denoted in blue and red, respectively; the range of optimization  $[f_{\min}, f_{\max}]$  is denoted by vertical dotted lines. (b): frequency evolution of the phase velocity; the horizontal dotted lines denote the phase velocity at zero and infinite frequency.

Figure A.11 illustrates the properties of the viscoelastic model. Figure A.11-(a) compares the reciprocal of the constant quality factor  $Q = 20$  with the value deduced from (A.1), for  $N = 2$  and  $N = 4$  relaxation mechanisms. Nonlinear optimization is performed from  $f_{\min} = 1$  kHz to  $f_{\max} = 100$  kHz. Large oscillations are obtained for  $N = 2$ ; excellent agreement is observed for  $N = 4$ . Figure A.11-(b) shows the increase in phase velocity from  $c_0 = \sqrt{E_R/\rho}$  to  $c_\infty = \sqrt{E/\rho}$ . The reader is referred to [5] for details about these quantities.

Lastly, the consistency relation (22) is proven here. Null attenuation amounts to an infinite quality factor. Equation (A.1) implies that  $Q = +\infty$  is obtained if  $\tau_{\varepsilon\ell} = \tau_{\sigma\ell}$ . In this case, the

viscoelastic coefficients (20) and (21) are

$$E_R = E, \quad K_{1\ell} = \frac{E}{N}, \quad K_{2\ell} = +\infty, \quad \eta_\ell = +\infty. \quad (\text{A.2})$$

To get a bounded stress, (18c) implies  $\varepsilon_{2\ell} = 0$ , and hence  $\varepsilon_{1\ell} = \varepsilon$  for  $\ell = 1, \dots, N$  (17). Putting together the total stress (16), the nonlinear elasticity (11) and the homogeneity property in (12), one obtains

$$\sigma = \sum_{\ell=1}^N s(\varepsilon_{1\ell}, K_{1\ell}, \mathbf{p}) = \sum_{\ell=1}^N s\left(\varepsilon, \frac{E}{N}, \mathbf{p}\right) = \frac{1}{N} \sum_{\ell=1}^N s(\varepsilon, E, \mathbf{p}) = s(\varepsilon, E, \mathbf{p}), \quad (\text{A.3})$$

which concludes the proof.

## Appendix B. Analysis of hyperbolicity

The Jacobian  $\mathbf{A}$  of  $\mathbf{f}$  (32) is

$$\mathbf{A}(\mathbf{U}) = \begin{pmatrix} 0 & 0 & \Phi_1 & \cdots & \Phi_N & 0 \\ -1 & 0 & 0 & \cdots & 0 & 0 \\ -1 & 0 & 0 & \cdots & 0 & 0 \\ \vdots & \vdots & \vdots & & \vdots & \vdots \\ -1 & 0 & 0 & \cdots & 0 & 0 \\ 0 & 0 & 0 & 0 & 0 & 0 \end{pmatrix}, \quad (\text{B.1})$$

where

$$\Phi_\ell = -\frac{1}{\rho} \frac{\partial \sigma_{1\ell}}{\partial \varepsilon_{1\ell}}. \quad (\text{B.2})$$

The determinant of  $\mathbf{A}$  writes

$$P_{\mathbf{A}}(\lambda) = -\lambda \begin{vmatrix} -\lambda & 0 & \Phi_1 & \cdots & \Phi_N \\ -1 & -\lambda & 0 & \cdots & 0 \\ -1 & 0 & -\lambda & & 0 \\ \vdots & & \ddots & \ddots & \\ -1 & & & 0 & -\lambda \end{vmatrix} \quad (\text{B.3})$$

The columns and lines are denoted by  $C_j$  and  $\mathcal{L}_j$ , respectively. The following algebraic manipulations are performed successively:

(i)  $C_1 \leftarrow \lambda C_1$ ,

(ii)  $C_1 \leftarrow C_1 - C_j$ , with  $j = 2, \dots, N+1$ ,

which yields

$$\begin{aligned} \lambda P_{\mathbf{A}}(\lambda) &= -\lambda \begin{vmatrix} -\lambda^2 - \sum_{\ell=1}^N \Phi_\ell & 0 & \Phi_1 & \cdots & \Phi_N \\ 0 & -\lambda & & & \\ \vdots & & & \ddots & \\ 0 & & & & -\lambda \end{vmatrix}, \\ &= (-1)^{N+1} \lambda^{N+2} \left( \lambda^2 + \sum_{\ell=1}^N \Phi_\ell \right). \end{aligned} \quad (\text{B.4})$$

453 It follows that the eigenvalues are 0 (with multiplicity  $N + 1$ ) and  $\pm c$ , with the sound velocity  
 454 (34). From (B.2), real eigenvalues are obtained if and only if  $c^2 > 0$  in (34).

455 Necessary and sufficient conditions are easily deduced from (34) for the models (13)-(15)  
 456 when  $N = 1$ : hyperbolicity is satisfied if  $|\varepsilon| < \varepsilon_c$ , where

$$\varepsilon_c = \begin{cases} d \left( \left( \frac{r+1}{a+1} \right)^{\frac{1}{r-a}} - 1 \right) & \text{(model 1),} \\ +\infty & \text{(model 2),} \\ \frac{1}{2\beta} \text{ if } \delta = 0, \quad \frac{\beta}{3\delta} \left( \sqrt{1 + \frac{3\delta}{\beta^2}} - 1 \right) \text{ otherwise} & \text{(model 3).} \end{cases} \quad (\text{B.5})$$

457 Model 2 is always hyperbolic. On the contrary, the widely-used Landau model (model 3) is  
 458 conditionally hyperbolic. When  $N > 1$ , the hyperbolicity condition  $|\varepsilon_{1\ell}| < \varepsilon_c$  is sufficient.

459 Given the nonlinear elastic models (13)-(15), the speed of sound  $c$  satisfies:

$$c^2 = \begin{cases} \sum_{\ell=1}^N \frac{K_{1\ell}}{\rho} \frac{1}{r-a} \left( \frac{r+1}{\left(1 + \frac{\varepsilon_{1\ell}}{d}\right)^r} - \frac{a+1}{\left(1 + \frac{\varepsilon_{1\ell}}{d}\right)^a} \right) & \text{(model 1),} \\ \sum_{\ell=1}^N \frac{K_{1\ell}}{\rho} \left( 1 - (r+a+3) \frac{\varepsilon_{1\ell}}{d} + \frac{1}{2} (r^2 + ra + a^2 + 6r + 6a + 11) \left( \frac{\varepsilon_{1\ell}}{d} \right)^2 \right) & \text{(model 2),} \\ \sum_{\ell=1}^N \frac{K_{1\ell}}{\rho} (1 - 2\beta \varepsilon_{1\ell} - 3\delta \varepsilon_{1\ell}^2) & \text{(model 3).} \end{cases} \quad (\text{B.6})$$

## 460 Appendix C. Analysis of the relaxation terms

461 For linear stress-strain relations (18), the relaxation coefficients (33) yield

$$\begin{cases} \frac{\partial \Delta_\ell}{\partial \varepsilon}(0) = \frac{1}{\eta_\ell} \sigma'_{2\ell}(0) = \frac{K_{2\ell}}{\eta_\ell}, \\ \frac{\partial \Delta_\ell}{\partial \varepsilon_{1\ell}}(0) = -\frac{1}{\eta_\ell} (\sigma'_{1\ell}(0) + \sigma'_{2\ell}(0)) = -\frac{1}{\eta_\ell} (K_{1\ell} + K_{2\ell}). \end{cases} \quad (\text{C.1})$$

462 The Jacobian matrix of the relaxation function (32) can be obtained

$$\mathbf{J} = \begin{pmatrix} 0 & 0 & \cdots & 0 & 0 \\ \frac{E_{21}}{\eta_1} & -\frac{E_{11} + E_{21}}{\eta_1} & & & 0 \\ \vdots & & \ddots & & \\ \frac{E_{2N}}{\eta_1} & & & -\frac{E_{1N} + E_{2N}}{\eta_N} & 0 \\ 0 & & \cdots & 0 & f_\xi \end{pmatrix}, \quad (\text{C.2})$$



with  $f_\xi = f_r$  if  $g > g_\sigma$ ,  $f_\xi = f_d$  if  $g < g_\sigma$ ,  $f_\xi = 0$  else. It follows that the eigenvalues are 0,  $-\frac{K_{1\ell} + K_{2\ell}}{\eta_\ell}$ , and  $-f_\xi$ .

#### Appendix D. Semi-analytical solution

The semi-analytical solution of the viscodynamic equations is computed as follows. Fourier transforms in space and time are applied to the system (56). Applying an inverse Fourier transform in space yields

$$\hat{v}(x, \omega) = \frac{i\omega \rho}{\sum_{\ell=1}^N K_{1\ell} \frac{i\omega + 1/\tau_{\varepsilon_\ell}}{i\omega + 1/\tau_{\sigma_\ell}}} \frac{\hat{\mathcal{G}}(\omega)}{2\pi} \int_{-\infty}^{+\infty} \frac{1}{k^2 - k_0^2} e^{-ikx_0} dk, \quad (\text{D.1})$$

where the hat refers to the Fourier transform,  $\mathcal{G}$  is the time evolution of the source, the relaxation times  $\tau_{\varepsilon_\ell}$  and  $\tau_{\sigma_\ell}$  are defined in (19), and  $k$  is the wavenumber. The poles  $\pm k_0$  satisfy

$$k_0^2 = \frac{\rho \omega^2}{\sum_{\ell=1}^N K_{1\ell} \frac{i\omega + 1/\tau_{\varepsilon_\ell}}{i\omega + 1/\tau_{\sigma_\ell}}} \quad (\text{D.2})$$

with  $\Im m(k_0) < 0$ . Applying the residue theorem gives the time-domain velocity

$$v(x, t) = \rho \int_0^\infty \Re e \left( \frac{\omega}{k_0} \frac{1}{\sum_{\ell=1}^N K_{1\ell} \frac{i\omega + 1/\tau_{\varepsilon_\ell}}{i\omega + 1/\tau_{\sigma_\ell}}} e^{-ik_0|x-x_0|} \hat{\mathcal{G}}(\omega) \right) d\omega. \quad (\text{D.3})$$

Expressions for  $\varepsilon$  and  $\varepsilon_{1\ell}$  can be obtained in a similar manner. Lastly, the numerical evaluation of (D.3) is done using a rectangular quadrature rule on  $N_f$  Fourier modes and with a constant frequency step  $\Delta f$  on the frequency band of interest.

- [1] J. D. ACHENBACH, *Wave Propagation in Elastic Solids*, North-Holland Publishing, Amsterdam (1973).
- [2] V. ALESHIN, K. E. A. VAN DEN ABEELE, *Microcontact-based theory for acoustics in microdamaged materials*, J. Mech. Phys. Solids, 55-2, (2007) 366-390.
- [3] V. ALESHIN, K. VAN DEN ABEELE, *Friction in unconforming grain contacts as a mechanism for tensorial stress-strain hysteresis*, J. Mech. Phys. Solids, 55-4, (2007) 765-787.
- [4] T. BOURBIÉ, O. COUSSY, B. ZINSZNER, *Acoustics of Porous Media*, Gulf Publishing Company (1987).
- [5] J. M. CARCIONE, *Wave Fields in Real Media: Wave Propagation in Anisotropic, Anelastic, Porous and Electromagnetic Media*, Elsevier (2007).
- [6] A. BEN JAZIA, B. LOMBARD, C. BELLIS, *Wave propagation in a fractional viscoelastic Andrade medium: diffusive approximation and numerical modeling*, Wave Motion, 51 (2014), 994-1010.
- [7] S. F. DAVIS, *Simplified second-order Godunov-type methods*, SIAM J. Sci. Stat. Comput., 9 (1988), 445-473.
- [8] S. Y. EMELIANOV, M. F. HAMILTON, Y. A. ILINSKII, E. A. ZABOLOTSKAYA, *Nonlinear dynamics of a gas bubble in an incompressible elastic medium*, J. Acoust. Soc. Am., 115-2 (2004), 581-588.
- [9] S. L. GAVRILYUK, V. M. TESHUKOV, *Generalized vorticity for bubbly liquid and dispersive shallow water*, Continuum Mech. Thermodyn., 13 (2001), 365-382.
- [10] S. K. GODUNOV, E. I. ROMENSKII, *Elements of Continuum Mechanics and Conservation Laws*, Springer (2003).

- [11] R. A. GUYER, P. A. JOHNSON, *Nonlinear mesoscopic elasticity: Evidence for a new class of materials*, Physics Today 52 (1999), 30-35.
- [12] R. A. GUYER, P. A. JOHNSON, *Nonlinear Mesoscopic Elasticity: The Complex Behaviour of Rocks, Solids, Concrete*, Wiley (2009).
- [13] M. F. HAMILTON, D. T. BLACKSTOCK, *Nonlinear Acoustics*, Academic Press (1998).
- [14] P. A. JOHNSON, B. ZINSNER, P. N. J. RASOLOFOSON, *Resonance and elastic nonlinear phenomena in rock*, J. Geophys. Res., 101 (1996), 11553-11564.
- [15] A. KADISH, J. A. TEN CATE, P. A. JOHNSON, *Frequency spectra of nonlinear elastic pulse-mode waves*, J. Acoust. Soc. Am., 100-3 (1996), 1375-1382.
- [16] A. V. LEBEDEV, L. A. OSTROVSKY, *A unified model of hysteresis and long-time relaxation in heterogeneous materials*, Acoustical Physics, 60-5 (2014), 555-561.
- [17] L. LANDAU, E. LIFSHITZ, *Theory of Elasticity*, Pergamon Press (1970).
- [18] R. J. LEVEQUE, *Finite Volume Methods for Hyperbolic Problems*, Cambridge University Press (2002).
- [19] R. J. LEVEQUE, D. H. YONG, *Solitary waves in layered nonlinear media*, SIAM J. Appl. Math., 63-5 (2003), 1539-1560.
- [20] B. LOMBARD, J. PIRAUX, *Numerical modeling of transient two-dimensional viscoelastic waves*, J. Comput. Phys., 230-15 (2011), 6099-6114.
- [21] S. NDANOU, N. FAVRIE, S. GAVRILYUK, *Criterion of hyperbolicity in hyperelasticity in the case of the stored energy in separable form*, J. Elast., 115 (2014), 1-25.
- [22] L. A. OSTROVSKY, P. A. JOHNSON, *Dynamic nonlinear elasticity in geomaterials*, Riv. Nuovo Cimento, 24- (2001), 1-46.
- [23] C. PECORARI, *Adhesion and nonlinear scattering by rough surfaces in contact: beyond the phenomenology of the Preisach-Mayergoyz framework*, J. Acoust. Soc. Am., 116-4 (2004), 1938-1947.
- [24] C. PECORARI, D. A. MENDELSON, *Forced nonlinear vibrations of a one-dimensional bar with arbitrary distributions of hysteretic damage*, J. Nondestruct. Eval., 33-2 (2014), 239-251.
- [25] G. RENAUD, P. Y. LE BAS, P. A. JOHNSON, *Revealing highly complex elastic nonlinear (anelastic) behavior of Earth materials applying a new probe: Dynamic acoustoelastic testing*, J. Geophys. Res., 117 (2012), B06202.
- [26] J. RIVIERE, G. RENAUD, R. A. GUYER, P. A. JOHNSON, *Pump and probe waves in dynamic acousto-elasticity: Comprehensive description and comparison with nonlinear elastic theories*, J. Appl. Phys., 114 (2013), 054905.
- [27] M. SCALERANDI, M. NOBILI, M. GRIFFA, A. S. GLIOZZI, F. BOSIA, *Preisach-Mayergoyz approach to fatigue-induced irreversibility*, Phys. Rev. B, 73 (2006), 092103.
- [28] M. SCALERANDI, A. S. GLIOZZI, C. L. E. BRUNO, P. ANTONACI, *Nonequilibrium and hysteresis in solids: disentangling conditioning from nonlinear elasticity*, Phys. Rev. B, 81 (2010), 104114.
- [29] J. A. TEN CATE, T. J. SHANKLAND, *Slow dynamics in the nonlinear elastic response of Berea sandstone*, Geophys. Res. Lett., 23-21 (1996), 3019-3022.
- [30] J. A. TEN CATE, E. SMITH, R. A. GUYER, *Universal slow dynamics in granular solids*, Phys. Rev. Lett., 85-5 (2000), 1020-1023.
- [31] E. F. TORO, *Riemann Solvers and Numerical Methods for Fluid Dynamics. A Practical Introduction*, Springer-Verlag (1999).
- [32] O. O. VAKHNENKO, V. O. VAKHNENKO, T. J. SHANKLAND, J. A. TEN CATE, *Strain-induced kinetics of intergrain defects as the mechanism of slow dynamics in the nonlinear resonant response of humid sandstone bars*, Phys. Rev. B, 70 (2004), 015602.
- [33] O. O. VAKHNENKO, V. O. VAKHNENKO, T. J. SHANKLAND, *Soft-ratchet modeling of end-point memory in the nonlinear resonant response of sedimentary rocks*, Physical Review B 71 (2005), 174103.
- [34] G. WHITHAM, *Linear and Nonlinear Waves*, Wiley-Interscience (1977).